JACS
JOURNAL OF THE AMERICAN CHEMICAL SOCIETY
pubs.acs.org/JACS
Article

Intermediate Binding Control Using Metal–Organic Frameworks Enhances Electrochemical CO_2 Reduction

Dae-Hyun Nam,[⊥] Osama Shekhah,[⊥] Geonhui Lee,[⊥] Arijit Mallick, Hao Jiang, Fengwang Li, Bin Chen, Joshua Wicks, Mohamed Eddaoudi,* and Edward H. Sargent*

Cite This: https://dx.doi.org/10.1021/jacs.0c10774

Read Online

ACCESS | Metrics & More | Article Recommendations | Supporting Information

ABSTRACT: In the electrochemical CO_2 reduction reaction (CO_2RR), control over the binding of intermediates is key for tuning product selectivity and catalytic activity. Here we report the use of reticular chemistry to control the binding of CO_2RR intermediates on metal catalysts encapsulated inside metal–organic frameworks (MOFs), thereby allowing us to improve CO_2RR electrocatalysis. By varying systematically both the organic linker and the metal node in a face-centered cubic (*fcu*) MOF, we tune the adsorption of CO_2, pore openness, and Lewis acidity of the MOFs. Using *operando* X-ray absorption spectroscopy (XAS) and *in situ* Raman spectroscopy, we reveal that the MOFs are stable under operating conditions and that this tuning plays the role of optimizing the *CO binding mode on the surface of Ag nanoparticles incorporated inside the MOFs with the increase of local CO_2 concentration. As a result, we improve the CO selectivity from 74% for Ag/Zr-*fcu*-MOF-1,4-benzenedicarboxylic acid (BDC) to 94% for Ag/Zr-*fcu*-MOF-1,4-naphthalenedicarboxylic acid (NDC). The work offers a further avenue to utilize MOFs in the pursuit of materials design for CO_2RR.

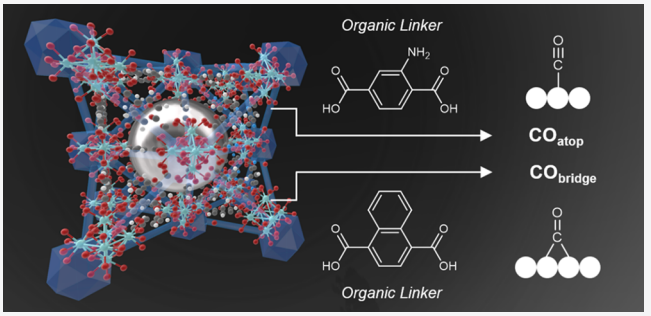

INTRODUCTION

The utilization of carbon dioxide (CO_2) is gaining interest in carbon capture and management.[1−3] The electrochemical CO_2 reduction reaction (CO_2RR) offers a pathway to its efficient utilization as feedstock for renewable electricity storage and conversion.[3] CO_2RR suffers from poor product selectivity and mixed products such as carbon monoxide (CO),[4] methane (CH_4),[5] methanol (CH_3OH),[6] formate ($HCOO^-$),[7] ethanol (C_2H_5OH),[8] and ethylene (C_2H_4),[9,10] widely reported in literature.[11]

Control over the binding of CO_2RR intermediates on the surface of an electrocatalyst can increase the Faradaic efficiency (FE), and decrease the overpotential, toward a desired product. Alloying,[12−14] doping,[15] metal/metal oxide interfaces,[16,17] grain boundaries,[18] and facets[19] have been used to achieve this control. However, currently, the CO_2RR performances such as selectivity to a desired product are still low, increasing cost for separation steps.

Metal–organic frameworks (MOFs), composed of organic linkers and metal nodes, have porous structures with spatially distributed metal atomic centers, and these interact efficiently with gaseous species and can be applied to selective gas adsorption/diffusion/storage.[20−23] For CO_2RR electrocatalysts, the metal atomic centers in the MOFs have been applied mostly as an active material.[24−29] For example, Co-porphyrin-based MOFs exhibited a high selectivity for CO production.[30] Also, the coordination number of Cu clusters formed from HKUST-1 was engineered for highly selective C_2H_4 production.[31] Despite these advances, the abundant reticular chemistry of MOFs offered by their great chemical flexibility of both organic linkers and metal nodes has not been explored yet in the electrochemical CO_2RR.

Here, we apply isoreticular MOFs to control reaction intermediate binding for efficient CO_2RR with high product selectivity. By functionalizing organic linkers with amine groups, directly changing the linkers, and altering the metal nodes, we tuned the CO_2 adsorption, pore openness, and Lewis acidity of a model Zr-face-centered cubic (*fcu*)-MOF and evaluated resulting impact on the CO_2RR properties of Ag nanoparticles encapsulated inside the MOF pores. We found that MOFs, chemically stable confirmed by *operando* X-ray absorption spectroscopy (XAS), promote product selectivity and decrease overpotential of the CO_2RR on Ag. Using *in situ* Raman spectroscopy, we found that the promoted stronger interaction by amine and enhanced physisorption by pore size-

Received: October 11, 2020

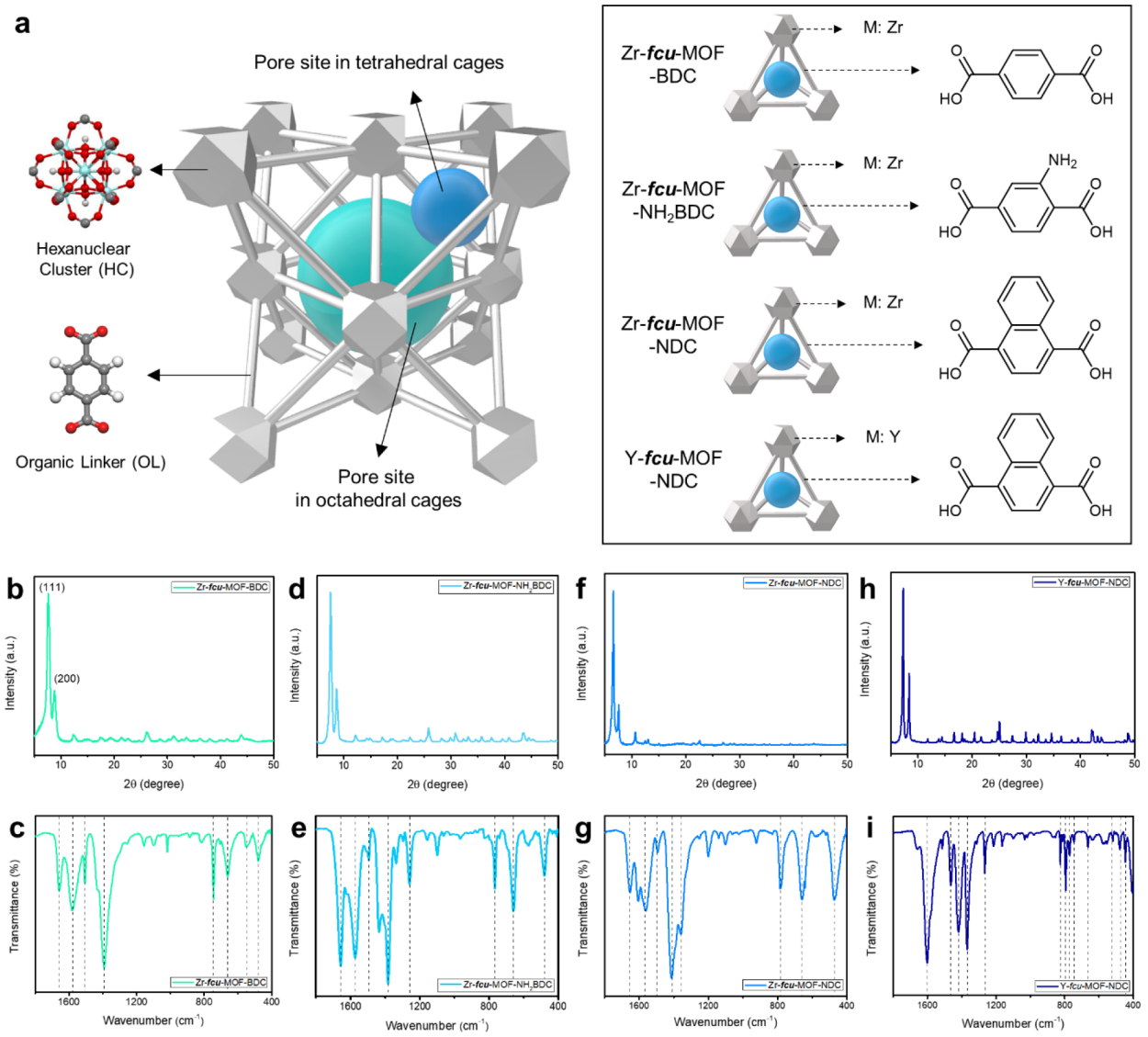

Figure 1. MOF design strategies to enhance the CO_2RR activity of Ag nanoparticles. (a) On the basis of the basic matrix of Zr-*fcu*-MOF-BDC, the MOFs are controlled by adding amine functional group ($-NH_2$) to organic linker, changing the organic linker to naphthalenedicarboxylic acid, and changing the element in metal node site from Zr to Y. The crystalline structures and functional groups in As-synthesized MOFs are investigated by XRD and FT-IR: (b, c) Zr-*fcu*-MOF-BDC, (d, e) Zr-*fcu*-MOF-NH_2BDC, (f, g) Zr-*fcu*-MOF-NDC, and (h, i) Y-*fcu*-MOF-NDC.

confinement of the MOFs can induce the promoted binding of *CO in atop or bridge modes. Levering the gas-phase species control in electrocatalysts with the aid of MOFs can help to steer the CO_2RR pathway toward desired products and add a degree of freedom in the design of next-generation of CO_2RR cathodes.

RESULTS AND DISCUSSION

MOF Design Strategy and Fabrication. Zr-*fcu*-MOF-BDC (UiO-66), a starting material, is synthesized via reaction between zirconium chloride ($ZrCl_4$) and 1,4-benzenedicarboxylic acid (1,4-BDC). In the unit cell of Zr-*fcu*-MOF-BDC, Zr ion-based hexanuclear clusters, which act as secondary building unit (SBU), are located at the face-centered cubic position of the MOF (Figure 1a). The connection between the SBU and organic linkers forms the pore sites at tetrahedral (blue) and octahedral (cyan) cages. To enhance CO_2 capture/interaction, the BDC organic linker of Zr-*fcu*-MOF-BDC was functionalized with an amine (NH_2-) group, which can provide stronger interaction with CO_2 (Zr-*fcu*-MOF-NH_2BDC). We changed 1,4-BDC to 1,4-naphthalenedicarboxylic acid (1,4-NDC) to enhance CO_2 capture via physisorption by decreasing the size of pore and pore-aperture size (Zr-*fcu*-MOF-NDC). The effect of Lewis acidity on CO_2RR activity was studied by changing the Zr-ion to a Y-ion in the hexanuclear cluster (Y-*fcu*-MOF-NDC).

Although these four types of MOFs share the same motif structure (*fcu*-MOF), we simulated each MOF structure, which can quantify the pore-aperture size and cage diameter, to find the effect of organic linker transition from 1,4-BDC to 1,4-NDC on the pore size confinement. Since the benzene rings of 1,4-BDC and 1,4-NDC can be rotated (Figure S1), the tetrahedral and octahedral cage diameters were calculated by averaging the cage diameters in both 0° and 90° rotated benzene ring positions (Figures S2–S5, Tables S1 and S2). Zr-*fcu*-MOF-BDC exhibited the highest porosity. Through amine group functionalization (Zr-*fcu*-MOF-NH_2BDC), the porosity decreased compared to Zr-*fcu*-MOF-BDC. When 1,4-BDC was

https://dx.doi.org/10.1021/jacs.0c10774
J. Am. Chem. Soc. XXXX, XXX, XXX−XXX

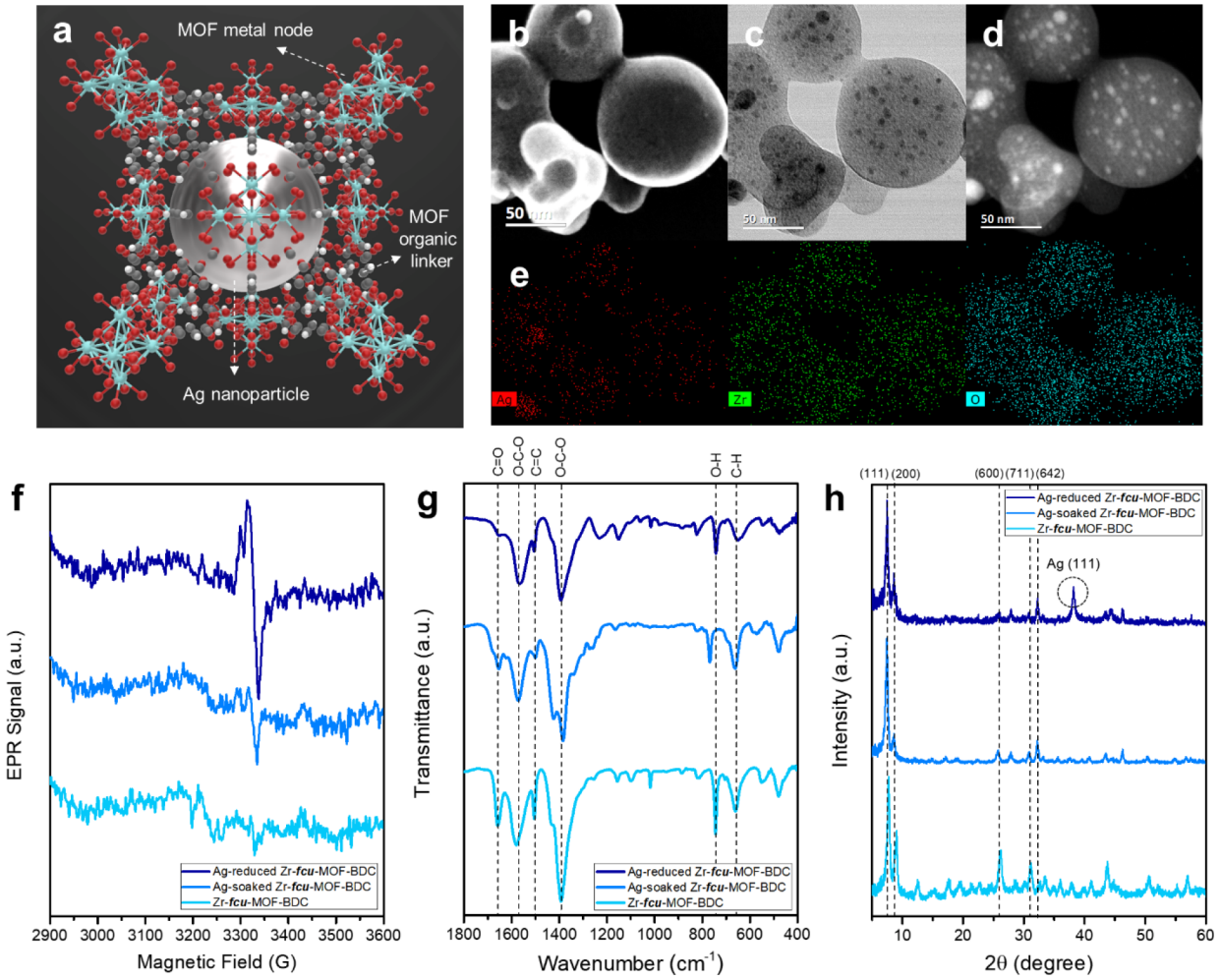

Figure 2. Metal nanoparticle incorporation at the pore site of MOFs. (a) Schematic for Ag nanoparticle incorporated MOF structure. The structure of encapsulated Ag nanoparticles in the pore of Zr-*fcu*-MOF-BDC is confirmed by (b) FE-SEM, (c) STEM BF, (d) STEM HAADF, and (e) STEM EDS images. Ag nanoparticles are incorporated by soaking the Zr-*fcu*-MOF-BDC with Ag^+ ions and reducing with using $NaBH_4$. The material status at each process is analyzed by (f) EPR, (g) FT-IR, and (h) XRD. .

substituted by 1,4-NDC (Zr-*fcu*-MOF-NDC), the maximum pore-aperture size and average tetrahedral, octahedral cage diameters were calculated as 5.0, 4.5, and 8.6 Å, respectively, which were lowest among the four MOF species. The porosity of Y-*fcu*-MOF-NDC was similar to that of Zr-*fcu*-MOF-NDC.

The crystallinity and chemical status of organic linkers in the synthesized MOFs were verified by X-ray diffraction (XRD) and Fourier transform infrared spectroscopy (FT-IR) (Figure 1b–i). The XRD patterns of the MOFs coincided with previous reports and simulation results, thus confirming the successful synthesis of each MOF in this work.[32−34] In the FT-IR of Zr-*fcu*-MOF-BDC, we observed the major peaks around 1660, 1656, 1583, 1506, 1395, 745, and 664 cm^{-1}, which indicate the C=O stretching vibration, carboxyl group coordinated with Zr^{4+}, O−C−O asymmetric stretching vibration, C=C vibration of benzene ring, O−C−O symmetric stretching vibration, O−H vibration, and C−H vibration in 1,4-BDC ligands, respectively (Figure 1c).[35] Similarities between Zr-*fcu*-MOF-BDC and Zr-*fcu*-MOF-NH_2BDC were verified by the XRD patterns and FT-IR peaks for 1,4-BDC ligands. However, the C=N peak at 1257 cm^{-1} and $-NH_2$ peak at 1618 cm^{-1} in the FT-IR of Zr-*fcu*-MOF-NH_2BDC differentiated it from Zr-*fcu*-MOF-BDC (Figure 1e).[36,37] The existence of 1,4-NDC in Zr-*fcu*-MOF-NDC and Y-*fcu*-MOF-NDC was confirmed by the relevant FT-IR peaks (Figure 1g,i).[38]

Active Material Incorporation into MOF. Using the electrochemical CO_2 conversion to CO as a model to understand the role of MOF supporter during CO_2RR, we fabricated Ag-incorporated MOFs (Figure 2a). We selected Ag for the model study since it is known to produce CO with high selectivity, and since it has weak binding with *CO, enabling study of the effect of MOF on intermediate binding control.[39] Ag is readily reduced selectively in MOFs that incorporate Ag compared to Zn. Ag nanoparticles were grown inside the pore sites of MOFs by a solution impregnation (soaking the MOFs with Ag^+ containing solution, and then reducing the Ag^+ with $NaBH_4$).[40] We incorporated Ag nanoparticles in all MOFs using the same methodology.

The size and distribution of incorporated Ag nanoparticles were analyzed with field-emission scanning electron microscope (FE-SEM) and transmission electron microscope (TEM). The spatial distribution of uniformly sized Ag nanoparticles (~5 nm) reveals the successful Ag incorporation because the nucleation and growth of Ag nuclei are confined by the dimensions of the MOF pore (Figure 2b–e). Ag nanoparticles formed not only in the interior pores but also on the exterior surfaces of the MOFs. Ag nanoparticles on the

https://dx.doi.org/10.1021/jacs.0c10774
J. Am. Chem. Soc. XXXX, XXX, XXX−XXX

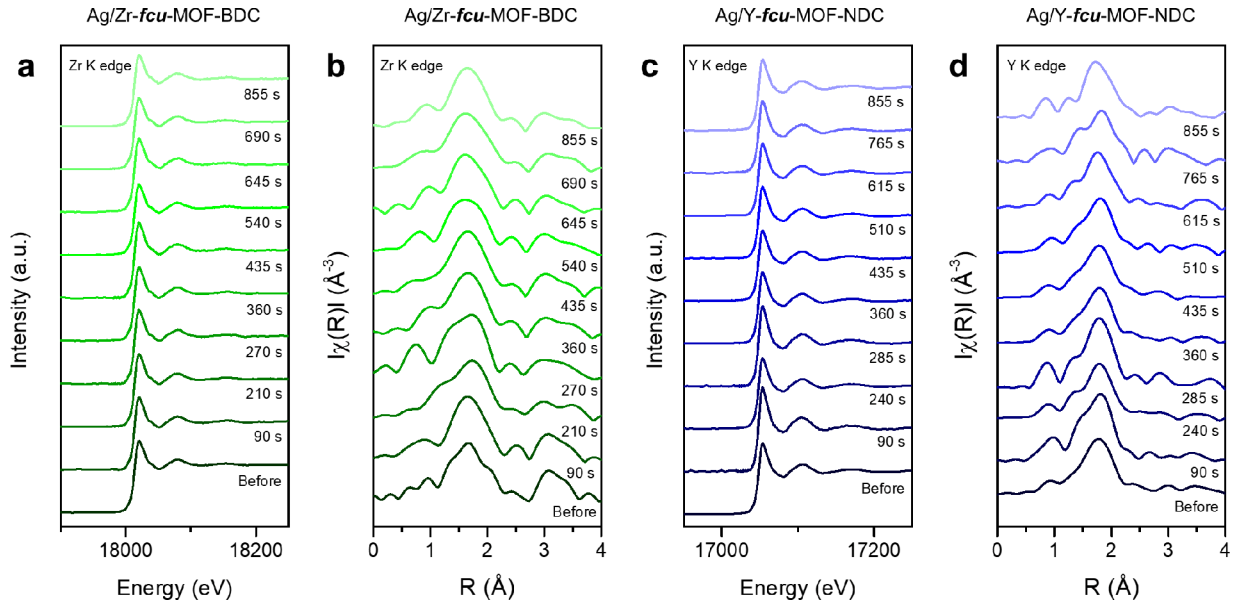

Figure 3. *Operando* XAS analysis to investigate the MOF status during the electrochemical CO_2RR. At the constant applied potential of −2.0 V versus Ag/AgCl in 0.5 M $KHCO_3$, the Zr K-edge (a) XANES and (b) EXAFS of Ag/Zr-***fcu***-MOF-BDC, and the Y K-edge (a) XANES and (b) EXAFS of Ag/Y-***fcu***-MOF-NDC were analyzed according to the catalytic reaction time. Oxidation states and coordinative structure information, investigated by XANES and EXAFS, reveal the stable MOF status during the CO_2RR.

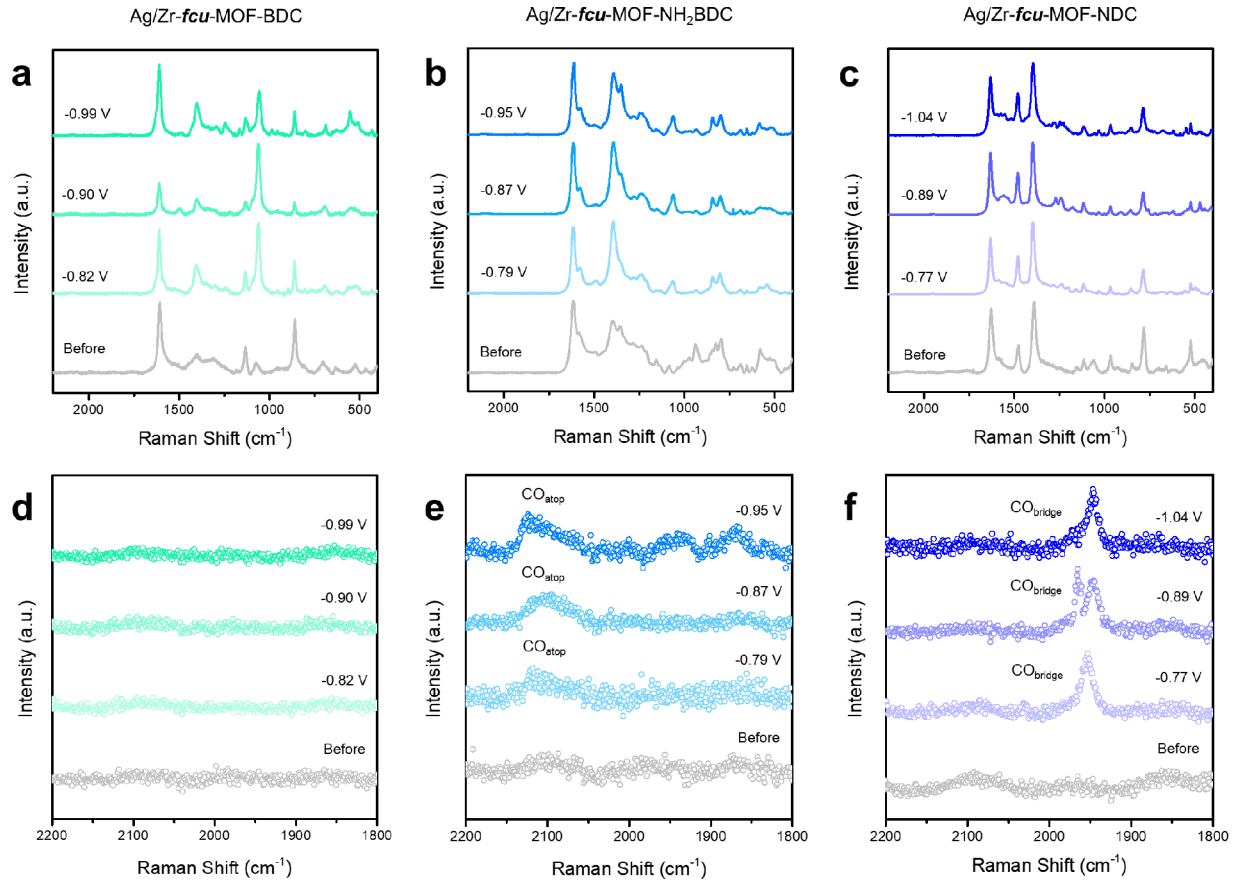

Figure 4. *In situ* Raman spectroscopy to investigate the status of MOF functional group evolution and *CO binding mode during CO_2RR. Raman spectra from 400 to 2200 cm^{-1} reveals the stability of MOF functional groups in (a) Ag/Zr-***fcu***-MOF-BDC, (b) Ag/Zr-***fcu***-MOF-NH_2BDC, and (c) Ag/Zr-***fcu***-MOF-NDC according to the reaction potentials. Magnified Raman spectra from 1800 to 2200 cm^{-1} show the CO intermediate binding mode at the catalysts of (d) Ag/Zr-***fcu***-MOF-BDC, (e) Ag/Zr-***fcu***-MOF-NH_2BDC, and (f) Ag/Zr-***fcu***-MOF-NDC.

exterior surface may contribute to enhance electrical conduction of the MOFs on the gas diffusion electrode (GDE).[41] The structures of the Ag nanoparticles were similar in both Zr- and Y-based MOFs (Figures S6–S8). The MOF

https://dx.doi.org/10.1021/jacs.0c10774
J. Am. Chem. Soc. XXXX, XXX, XXX−XXX

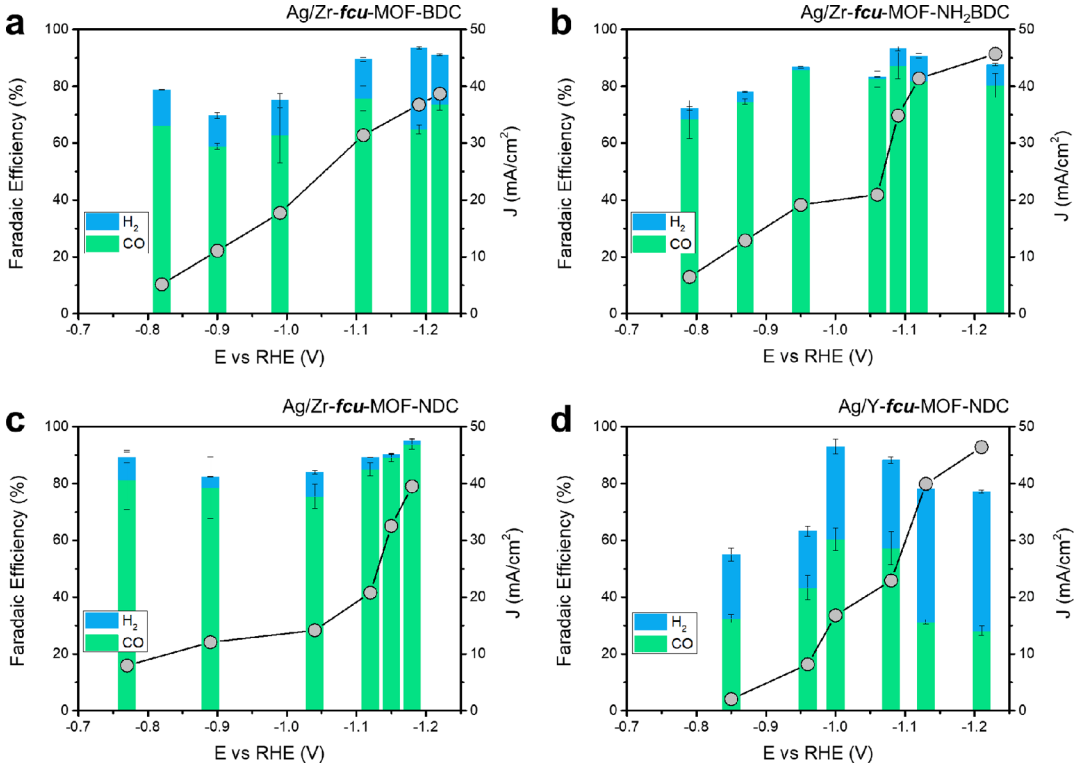

Figure 5. CO_2RR catalytic activity of Ag-incorporated MOFs. Electrochemical CO_2RR products of (a) Ag/Zr-*fcu*-MOF-BDC, (b) Ag/Zr-*fcu*-MOF-NH_2BDC, (c) Ag/Zr-*fcu*-MOF-NDC, and (d) Ag/Y-*fcu*-MOF-NDC were investigated according to the potential in the flow cell electrolyzer with the electrolyte of 0.5 M $KHCO_3$.

control will mainly affect the CO_2RR behavior of the interior Ag nanoparticles that exhibit higher surface to volume ratio and number of nanoparticles compared to exterior one. The outer morphology of the MOFs that incorporate Ag was affected by the type of organic linkers (Figure S9).[42] Furthermore, X-ray photoelectron spectroscopy (XPS) exhibited identical oxidation states of Ag and other elements in all MOFs studied herein (Figure S10).

The reduction of Ag^+ and the material stability of MOF during the fabrication were investigated using electron paramagnetic resonance (EPR), FT-IR, and XRD. Unlike the bare MOF, Ag^+-soaked Zr-*fcu*-MOF-BDC exhibited a clear EPR signal. We confirmed the reduction of Ag^+ to metallic Ag during solution impregnation by the increased EPR peak intensity (Figure 2f).[43] The major FT-IR peaks of Zr-*fcu*-MOF-BDC (C=O, O−C−O, C=C, O−H, and C−H) were maintained during the sequential Ag^+ incorporation and reduction process (Figure 2g). Additionally, the formation of Ag nanoparticles and the MOF stability during the fabrication have been confirmed through XRD, which indicates the existence of (111) main peak for Ag (Figure 2h).

MOF Stability during CO_2RR. We investigated the stability of Ag-incorporated MOFs during CO_2RR by *operando* XAS at an applied potential of −2.0 versus Ag/AgCl (Figure 3) in 0.5 M $KHCO_3$. We tracked the oxidation states and atomic structures (coordination number and atomic distance) of the elements in the metal node of MOFs with X-ray absorption near edge structure (XANES) and extended X-ray absorption fine structure (EXAFS). There was no observed difference between the "before reaction" and "during reaction" states in both XANES and EXAFS of the Zr K-edge in Ag/Zr-*fcu*-MOF-BDC (Figure 3a,b). This was confirmed clearly when we compared XANES spectra with standard metal and metal oxide (Figure S11a,c). Combined with the identical peak position of derivative normalized $x\mu$(E), these results indicated a constant Zr oxidation state, coordination number, and atomic distance around the Zr atoms in Zr-based MOFs during the reaction (Figure S12). This trend was similar in the Y K-edge XANES and EXAFS of Ag/Y-*fcu*-MOF-NDC (Figure 3c,d). If MOFs were changed by the reduction of metal node in SBU of MOFs during CO_2RR, there should be an increase of *operando* EXAFS peak intensity for metal−metal bonding and a suppression of *operando* EXAFS peak intensity for metal−oxygen bonding.[31] However, in this work, there was no remarkable increase in *operando* EXAFS peak intensity for metal−metal bonding and decrease in *operando* EXAFS peak intensity for metal−oxygen bonding in Ag/Zr-*fcu*-MOF-BDC and Ag/Y-*fcu*-MOF-NDC (Figure S11b,d). These observations suggest that the Zr- and Y-based MOFs in this work are stable during CO_2RR.

Intermediates Binding Control by MOF. To identify the function of the MOF supporter on the cathode, we used *in situ* Raman spectroscopy to track, in real time, the binding of intermediates on the catalyst surface (Figure 4). Raman spectra were collected before and during the reaction according to a series of applied potentials. As the reference, the Raman spectra of Zr-*fcu*-MOF-BDC, Zr-*fcu*-MOF-NH_2BDC, Zr-*fcu*-MOF-NDC, and Y-*fcu*-MOF-NDC were measured without Ag species (Figure S13). Matching it with the Raman spectra in Figure 4a−c, the Raman peaks from MOFs can be distinguished with those from Ag species. In all cases, there was no difference in the Raman peak according to the applied potential in 0.5 M $KHCO_3$, and this also supports the superior MOF stability during CO_2RR.

https://dx.doi.org/10.1021/jacs.0c10774
J. Am. Chem. Soc. XXXX, XXX, XXX−XXX

The clear difference between MOF species was observed at the Raman shift from 1800 to 2200 cm^{-1}, which corresponds to the *CO binding mode. In the bare Ag/Zr-*fcu*-MOF-BDC, there was no peak in this range (Figure 4d). This phenomenon can be interpreted as *CO desorption during CO_2RR:[44] indeed, in general, the binding energy between Ag and CO is low, and this has been observed in *in situ* Raman of Ag/Zr-*fcu*-MOF-BDC.[39,45] However, in the NH_2-functionalized Ag/Zr-*fcu*-MOF-NH_2BDC, the broad peaks were observed in the region around 2100 cm^{-1}, which indicates the C≡O stretching mode of CO_{atop} molecules (Figure 4e).[46,47] In the *in situ* Raman of pore size-confined Ag/Zr-*fcu*-MOF-NDC, narrow peaks were observed at 1950 cm^{-1}, which indicates the C≡O stretching mode of CO_{bridge} molecules (Figure 4f).[46,47] The existence of *CO Raman peaks in both Ag/Zr-*fcu*-MOF-NH_2BDC and Ag/Zr-*fcu*-MOF-NDC can be interpreted as the increased local CO_2 concentration near active materials by the NH_2-functionalization and pore size confinement of the MOF. In the case of Ag/Y-*fcu*-MOF-NDC with decreased Lewis acidity compared to Zr-based MOFs, the Raman peaks for CO intermediates were not observed (Figure S14). This shows that the binding mode control of the intermediates is effective when the Lewis acidity environment is well-prepared for CO_2RR.

As the local CO_2 concentration is increased via the action of the MOFs, the local pH in $KHCO_3$ can be decreased.[48] There is also a possibility that the *CO binding mode can be controlled by the local pH change; the increase in local pH can increase CO_{bridge} population on Ni, Co, Pt, and Cu electrodes.[47] Reticular chemistry-based *CO binding mode control can potentially be extended further by varying electrolytes and active materials with systematic MOF design.

CO_2RR of Active Material-Incorporated MOFs. The electrochemical CO_2RR performance of Ag nanoparticle-incorporated MOFs was investigated using a GDE where CO_2 is supplied directly to the catalyst. The gaseous products were analyzed under chronoamperometric operation and in a neutral electrolyte of 0.5 M $KHCO_3$ (Figure S15). We confirm that Ag is the active material for CO_2RR of Ag-incorporated MOFs because H_2 was major products upon using bare MOFs without Ag (Figure S16).

In the bare MOF (Ag/Zr-*fcu*-MOF-BDC), main CO_2RR products were identified as CO and hydrogen (H_2), as is typical of Ag active materials (Figure 5a). The CO FE was mostly lower than 74% and H_2 FE increased from 13% to 29% as the potential increased toward the range enabling high current densities around 40 mA/cm^2. In the NH_2-functionalized MOFs (Ag/Zr-*fcu*-MOF-NH_2BDC) and pore size-confined MOFs (Ag/Zr-*fcu*-MOF-NDC), the overall CO_2RR activities were enhanced compared to the bare MOF. The overpotentials decreased, and the CO_2RR were more dominant than the hydrogen evolution reaction (HER). In the Ag/Zr-*fcu*-MOF-NH_2BDC, the CO FE increased to over 80%, and H_2 FE decreased to lower than 8% (Figure 5b). Especially, the H_2 FE was extremely low in the potential range lower than −1.0 V versus RHE. The amine group in Ag/Zr-*fcu*-MOF-NH_2BDC can induce the formation of carbamate intermediate, promoting CO_2RR activity.[49] The enhanced CO FE can be explained by the increase of local CO_2 concentration and the formation of carbamate.[42,49] In the Ag/Zr-*fcu*-MOF-NDC, the enhanced CO_2RR performance in terms of CO and H_2 FE was similar to that of Ag/Zr-*fcu*-MOF-NH_2BDC (Figure 5c). In the potential range for CO_2RR of Ag/Zr-*fcu*-MOF-NDC more negative than −1.0 V versus RHE, the CO FE increased to 94% and H_2 FE decreased to 1%. This indicates higher CO selectivity than that of Ag/Zr-*fcu*-MOF-NH_2BDC. Recently, it was reported that CO_{bridge} are inert and do not participate in the reaction, unlike CO_{atop}.[47] The inertness of CO_{bridge} in Ag/Zr-*fcu*-MOF-NDC may enhanced the CO selectivity in the CO_2RR of Ag active materials compared to CO_{atop} in Ag/Zr-*fcu*-MOF-NH_2BDC. The difference in CO binding modes, specifically between CO_{atop} and CO_{bridge}, controlled by modifying the MOF functional group and porosity, might affect the CO selectivity of Ag nanoparticles located at the pore site of the Zr-based MOFs. When the metal node was changed from Zr to Y, the CO_2RR performance of Ag/Y-*fcu*-MOF-NDC was lower even in the similar pore structure with Ag/Zr-*fcu*-MOF-NDC (Figure 5d). This is due to the decrease in Lewis acidity and the change in the framework overall charge from neutral (Zr-*fcu*-MOF-NDC) to cationic (Y-*fcu*-MOF-NDC).

The TEM images of MOFs that incorporate Ag indicate the coexistence of Ag nanoparticles in the interior pores and on the exterior surface of the MOFs. We observed more interior Ag than exterior Ag. The surface to volume ratio of interior Ag is higher in view of its size and number. Therefore, we expect that the effect of MOFs will be dominated by the effect of interior Ag.

We investigated the structures of Ag nanoparticles in Ag-incorporated MOFs by TEM after 1 h CO_2RR at −2.4 V versus Ag/AgCl. Ag/Zr-*fcu*-MOF-NH_2BDC and Ag/Zr-*fcu*-MOF-NDC exhibited good stability by suppressing HER (Figure S17). We found that interior Ag nanoparticles maintain their structure, a finding we associate with the confinement effect of the MOF pores. In the case of exterior Ag nanoparticles, we found that reconstruction of Ag nanoparticles occurs during CO_2RR (Figure S18).

■ CONCLUSION

We present a new approach to utilize MOF materials to control the binding mode of CO_2RR intermediates, thus modulating the product selectivity and activity of the reaction. Starting from a material design with reticular chemistry, we studied the effect of capturing CO_2 near the active site and modifying Lewis acidity on CO_2RR performance by utilizing isoreticular MOFs as a support. This was enabled by adding amine functional group (Zr-*fcu*-MOF-NH_2BDC), and changing the organic linker (Zr-*fcu*-MOF-NDC) and metal node (Y-*fcu*-MOF-NDC) from the bare Zr-*fcu*-MOF-BDC. The increase of local CO_2 concentration near the Ag nanoparticles by MOF supporters enhanced CO_2RR while it suppressed HER. Furthermore, we found that atop and bridge binding modes of CO intermediates can be modulated by the NH_2-functionalized and pore size-confined MOF species; CO_{atop}/CO_{bridge} control is crucial for determining the product selectivity. Away from the conventional approach to controlling the binding energy between active materials and CO_2RR intermediates, this work paves the way for improving CO_2RR activity and product selectivity by directly interacting with the gaseous intermediates and controlling their binding mode.

■ EXPERIMENTAL SECTION

Synthesis of Isoreticular MOFs. *Synthesis of Zr-*fcu*-MOF-BDC.* Zr-*fcu*-MOF-BDC was synthesized by dissolving $ZrCl_4$ (0.053 g, 0.227 mmol,) and 1,4-benzene-dicarboxylic acid (H_2BDC) (0.034 g, 0.227 mmol) in 6 mL DMF at room temperature in a 15 mL glass vial. Then 1 mL of acetic acid was added to the resulting mixture, and

https://dx.doi.org/10.1021/jacs.0c10774
J. Am. Chem. Soc. XXXX, XXX, XXX−XXX

it was placed in a preheated oven at 120 °C for 24 h. After the reaction mixture was cooled in air to room temperature, the resulting solid was filtered, repeatedly washed with DMF, and dried at room temperature.

*Synthesis of Zr-**fcu**-MOF-NH_2BDC.* Synthesis of Zr-*fcu*-MOF-NH_2BDC was performed by dissolving $ZrCl_4$ (1.50 g, 6.4 mmol), 2-amino-1,4-benzenedicarboxylic acid (H_2N−BDC) (1.5 g, 6.4 mmol), and 5 mL of acetic acid in DMF (150 mL) at room temperature in a 500 mL volumetric flask. The resulting mixture was placed in a preheated oven at 120 °C for 24 h. After the solution was cooled to room temperature in air, the resulting solid was filtered and repeatedly washed with absolute hot ethanol (~60 °C) for 3 days. The resulting yellow powder was filtered and dried under vacuum at ambient temperature.

*Synthesis of Zr-**fcu**-MOF-NDC.* Synthesis of Zr-*fcu*-MOF-NDC was performed by dissolving $ZrCl_4$ (0.053 g, 0.227 mmol) and naphthalene 1,4-dicarboxylic acid (50 mg, 0.231 mmol) mixed in 10 mL of DMF. Then 2 mL of acetic acid was added to the mixture and heated for 24 h at 120 °C in a preheated oven. After that, the white ppt was centrifuged and washed thrice with DMF and after 1 day three times with acetone. Then it was dried and used for the next purpose.

*Synthesis of Y-**fcu**-MOF-NDC.* The 1,4-H_2NDC (9.41 mg, 0.0435 mmol), $Y(NO_3)_3{\cdot}5H_2O$ (19.15 mg, 0.0515 mmol), 2-fluorobenzoic acid (48.7 mg, 0.348 mmol), DMF (2.2 mL), H_2O (0.5 mL), and HNO_3 (0.3 mL, 3.5 M in DMF) were combined in a 20 mL scintillation vial, sealed, and heated to 115 °C for 60 h and cooled to room temperature. The polyhedral crystals were collected and air-dried. The as-synthesized sample of Y-*fcu*-MOF-NDC was washed with 10 mL of anhydrous DMF and immersed in 10 mL of ethanol for 7 days, during which time the ethanol was replaced three times per day.

Metal Incorporation at the MOF Pore Site. Silver nitrate ($AgNO_3$, 100 mg) was dissolved in the 2 mL acetonitrile solution. Then 100 mg of powders of each MOF (Zr-*fcu*-MOF-BDC, Zr-*fcu*-MOF-NH_2BDC, Zr-*fcu*-MOF-NDC, Y-*fcu*-MOF-NDC) was immersed in the $AgNO_3$ containing acetonitrile solution and stirred at the room temperature for 12 h. After centrifuging, Ag^+-soaked MOF was dried in the vacuum oven overnight. Ag^+-soaked MOF was dispersed and stirred in 0.6 mmol/mL $NaBH_4$ containing ethanol solution for the reduction of Ag^+. After centrifuging, Ag incorporated MOF was dried in the vacuum overnight.

Material Characterization. Powder X-ray diffraction (PXRD) measurements were carried out at room temperature on a PANalytical X'Pert PRO diffractometer 45 kV, 40 mA for Cu Kα (λ = 1.5418 Å), with a scan speed of 1.0° min^{-1} and a step size of 0.02° in 2θ. Also, Rigaku MiniFlex 600 diffractometer with Copper Kα radiation (λ = 1.5406 Å) was applied for PXRD. FT-IR was carried out by Thermo Scientific iS50 with the spectral range of 4600−50 cm^{-1}. XPS for investigating the Ag, Zr, Y, and O oxidation status was carried out by Thermo Scientific Al Kα source XPS system with a spot size of 400 μm. SEM and TEM analyses for structure characterization were carried out by a Hitachi FE-SEM S-5200 and Hitachi CFE-TEM HF3300. The local atomic structure was measured by EPR. It was carried out by a Bruker ECS-EMX X-band EPR spectrometer at the room temperature of 300 K. DPPH (2,2-diphenyl-1-picrylhydrazyl) was used for standardization of the peak position and intensity of EPR signal.

Electrochemical CO_2 Reduction. CO_2RR performance of Ag incorporated MOF was evaluated in a flow cell. It was composed of Ag-incorporated MOF on gas diffusion layer (GDL) as a cathode, Ni foam as an anode, and Ag/AgCl (3 M KCl) as a reference electrode. The cathode was made by spray coating the Ag-incorporated MOF containing ink (nafion + methanol). In the flow cell, 0.5 M $KHCO_3$ electrolyte was flowed in cathode and anode independently separated by anion exchange membrane. CO_2 gas flowed with a rate of 50 sccm. Chronoamperometry at the constant potential was performed by electrochemical station (Autolab). The electrode potentials were converted to RHE based on the following equation: $E_{RHE} = E_{Ag/AgCl} + 0.210\ V + 0.059 \times pH + iR$ (with iR-correction) The collected gaseous products during CO_2RR were analyzed in 1 mL volumes by a gas chromatograph (PerkinElmer Clarus 600) with a thermal conductivity detector (TCD) and a flame ionization detector (FID).

***In Situ*/*Operando* Spectroscopy.** XAS measurements at the Cu K-edge were performed at 9-BM beamline of the Advanced Photon Source (APS, Argonne National laboratory, IL). *Operando* XAS measurements were performed by using a custom flow cell in 0.5 M $KHCO_3$ electrolyte with CO_2 gas flowing from the backside of a gas diffusion layer. *Operando* XANES and EXAFS scan data were collected during the cell operation mode of chronoamperometry at the potential of −2.0 V versus Ag/AgCl, same with the CO_2RR activity measurement condition. *In situ* Raman was carried out by a Renishaw inVia Raman Microscope (obsective lense: 63×, 785 nm laser) with the liquid-electrolyte gas flow cell.

■ ASSOCIATED CONTENT

Supporting Information

The Supporting Information is available free of charge at https://pubs.acs.org/doi/10.1021/jacs.0c10774.

Detailed information on simulation of pore structures of MOFs, structure investigation, XPS analysis, XAS analysis, Raman spectra, chronoamperometry, stability, liquid product analysis for CO_2RR performance measurement (PDF)

■ AUTHOR INFORMATION

Corresponding Authors

Edward H. Sargent − *Department of Electrical and Computer Engineering, University of Toronto, Toronto, Ontario M5S 3G4, Canada;* orcid.org/0000-0003-0396-6495; Email: ted.sargent@utoronto.ca

Mohamed Eddaoudi − *Division of Physical Sciences and Engineering, Advanced Membranes and Porous Materials Center, Functional Materials Design, Discovery and Development Research Group (FMD3), King Abdullah University of Science and Technology (KAUST), Thuwal 23955-6900, Kingdom of Saudi Arabia;* orcid.org/0000-0003-1916-9837; Email: mohamed.eddaoudi@kaust.edu.sa

Authors

Dae-Hyun Nam − *Department of Electrical and Computer Engineering, University of Toronto, Toronto, Ontario M5S 3G4, Canada;* orcid.org/0000-0002-0871-1355

Osama Shekhah − *Division of Physical Sciences and Engineering, Advanced Membranes and Porous Materials Center, Functional Materials Design, Discovery and Development Research Group (FMD3), King Abdullah University of Science and Technology (KAUST), Thuwal 23955-6900, Kingdom of Saudi Arabia;* orcid.org/0000-0003-1861-9226

Geonhui Lee − *Department of Electrical and Computer Engineering, University of Toronto, Toronto, Ontario M5S 3G4, Canada*

Arijit Mallick − *Division of Physical Sciences and Engineering, Advanced Membranes and Porous Materials Center, Functional Materials Design, Discovery and Development Research Group (FMD3), King Abdullah University of Science and Technology (KAUST), Thuwal 23955-6900, Kingdom of Saudi Arabia*

Hao Jiang − *Division of Physical Sciences and Engineering, Advanced Membranes and Porous Materials Center, Functional Materials Design, Discovery and Development Research Group (FMD3), King Abdullah University of*

https://dx.doi.org/10.1021/jacs.0c10774
J. Am. Chem. Soc. XXXX, XXX, XXX−XXX

Science and Technology (KAUST), Thuwal 23955-6900, Kingdom of Saudi Arabia; orcid.org/0000-0002-1234-624X

Fengwang Li − *Department of Electrical and Computer Engineering, University of Toronto, Toronto, Ontario M5S 3G4, Canada;* orcid.org/0000-0003-1531-2966

Bin Chen − *Department of Electrical and Computer Engineering, University of Toronto, Toronto, Ontario M5S 3G4, Canada*

Joshua Wicks − *Department of Electrical and Computer Engineering, University of Toronto, Toronto, Ontario M5S 3G4, Canada*

Complete contact information is available at: https://pubs.acs.org/10.1021/jacs.0c10774

Author Contributions

[⊥]D.-H.N., O.S., and G.L. contributed equally to this work.

Notes

The authors declare no competing financial interest.

■ ACKNOWLEDGMENTS

This publication is based upon work supported by the King Abdullah University of Science and Technology (KAUST) Office of Sponsored Research (OSR) under Award No. OSR-2018-CPF-3665-03. This research used synchrotron resources of the Advanced Photon Source (APS), an Office of Science User Facility operated for the US Department of Energy Office of Science by Argonne National Laboratory and was supported by the US Department of Energy under Contract No. DE-AC02-06CH11357 and the Canadian Light Source and its funding partners. The authors thank Dr. T. P. Wu, Dr. Y. Z. Finfrock, Dr. G. Sterbinsky, and Dr. L. Ma for technical support at 9-BM beamline of APS. The authors acknowledge the use of facilities within CFI-funded Ontario Centre for the Characterization of Advanced Materials at the University of Toronto. This research was supported by the program of Carbon to X technology development for production of useful substances (2020M3H7A1098376), through the National Research Foundation of Korea (NRF), funded by the Korean government (Ministry of Science and ICT (MSIT)).

■ REFERENCES

(1) De Luna, P.; Hahn, C.; Higgins, D.; Jaffer, S. A.; Jaramillo, T. F.; Sargent, E. H. What Would It Take for Renewably Powered Electrosynthesis to Displace Petrochemical Processes? *Science* **2019**, *364* (6438), No. eaav3506.

(2) Birdja, Y. Y.; Pérez-Gallent, E.; Figueiredo, M. C.; Göttle, A. J.; Calle-Vallejo, F.; Koper, M. T. M. Advances and Challenges in Understanding the Electrocatalytic Conversion of Carbon Dioxide to Fuels. *Nat. Energy* **2019**, *4* (9), 732−745.

(3) Nitopi, S.; Bertheussen, E.; Scott, S. B.; Liu, X.; Engstfeld, A. K.; Horch, S.; Seger, B.; Stephens, I. E. L.; Chan, K.; Hahn, C.; Nørskov, J. K.; Jaramillo, T. F.; Chorkendorff, I. Progress and Perspectives of Electrochemical CO_2 Reduction on Copper in Aqueous Electrolyte. *Chem. Rev.* **2019**, *119* (12), 7610−7672.

(4) Liu, M.; Pang, Y.; Zhang, B.; De Luna, P.; Voznyy, O.; Xu, J.; Zheng, X.; Dinh, C.-T.; Fan, F.; Cao, C.; García de Arquer, F. P.; Safaei, T. S.; Mepham, A.; Klinkova, A.; Kumacheva, E.; Filleter, T.; Sinton, D.; Kelley, S. O.; Sargent, E. H. Enhanced Electrocatalytic CO_2 Reduction via Field-Induced Reagent Concentration. *Nature* **2016**, *537*, 382−386.

(5) Li, Y.; Cui, F.; Ross, M. B.; Kim, D.; Sun, Y.; Yang, P. Structure-Sensitive CO_2 Electroreduction to Hydrocarbons on Ultrathin 5-Fold Twinned Copper Nanowires. *Nano Lett.* **2017**, *17* (2), 1312−1317.

(6) Yang, H.; Wu, Y.; Li, G.; Lin, Q.; Hu, Q.; Zhang, Q.; Liu, J.; He, C. Scalable Production of Efficient Single-Atom Copper Decorated Carbon Membranes for CO_2 Electroreduction to Methanol. *J. Am. Chem. Soc.* **2019**, *141* (32), 12717−12723.

(7) Klinkova, A.; De Luna, P.; Dinh, C.-T.; Voznyy, O.; Larin, E. M.; Kumacheva, E.; Sargent, E. H. Rational Design of Efficient Palladium Catalysts for Electroreduction of Carbon Dioxide to Formate. *ACS Catal.* **2016**, *6* (12), 8115−8120.

(8) Li, Y. C.; Wang, Z.; Yuan, T.; Nam, D.-H.; Luo, M.; Wicks, J.; Chen, B.; Li, J.; Li, F.; de Arquer, F. P. G.; Wang, Y.; Dinh, C.-T.; Voznyy, O.; Sinton, D.; Sargent, E. H. Binding Site Diversity Promotes CO_2 Electroreduction to Ethanol. *J. Am. Chem. Soc.* **2019**, *141* (21), 8584−8591.

(9) Dinh, C.-T.; Burdyny, T.; Kibria, M. G.; Seifitokaldani, A.; Gabardo, C. M.; García de Arquer, F. P.; Kiani, A.; Edwards, J. P.; De Luna, P.; Bushuyev, O. S.; Zou, C.; Quintero-Bermudez, R.; Pang, Y.; Sinton, D.; Sargent, E. H. CO_2 Electroreduction to Ethylene via Hydroxide-Mediated Copper Catalysis at an Abrupt Interface. *Science* **2018**, *360* (6390), 783−787.

(10) Li, F.; Thevenon, A.; Rosas-Hernández, A.; Wang, Z.; Li, Y.; Gabardo, C. M.; Ozden, A.; Dinh, C. T.; Li, J.; Wang, Y.; Edwards, J. P.; Xu, Y.; McCallum, C.; Tao, L.; Liang, Z.-Q.; Luo, M.; Wang, X.; Li, H.; O'Brien, C. P.; Tan, C.-S.; Nam, D.-H.; Quintero-Bermudez, R.; Zhuang, T.-T.; Li, Y. C.; Han, Z.; Britt, R. D.; Sinton, D.; Agapie, T.; Peters, J. C.; Sargent, E. H. Molecular Tuning of CO_2-to-Ethylene Conversion. *Nature* **2020**, *577*, 509−513.

(11) Hori, Y. Electrochemical CO_2 Reduction on Metal Electrodes BT - Modern Aspects of Electrochemistry; Vayenas, C. G., White, R. E., Gamboa-Aldeco, M. E., Eds.; Springer New York: New York, 2008; pp 89−189.

(12) Wang, X.; Wang, Z.; Zhuang, T.-T.; Dinh, C.-T.; Li, J.; Nam, D.-H.; Li, F.; Huang, C.-W.; Tan, C.-S.; Chen, Z.; Chi, M.; Gabardo, C. M.; Seifitokaldani, A.; Todorović, P.; Proppe, A.; Pang, Y.; Kirmani, A. R.; Wang, Y.; Ip, A. H.; Richter, L. J.; Scheffel, B.; Xu, A.; Lo, S.-C.; Kelley, S. O.; Sinton, D.; Sargent, E. H. Efficient Upgrading of CO to C_3 Fuel Using Asymmetric C-C Coupling Active Sites. *Nat. Commun.* **2019**, *10* (1), 5186.

(13) Ma, S.; Sadakiyo, M.; Heima, M.; Luo, R.; Haasch, R. T.; Gold, J. I.; Yamauchi, M.; Kenis, P. J. A. Electroreduction of Carbon Dioxide to Hydrocarbons Using Bimetallic Cu-Pd Catalysts with Different Mixing Patterns. *J. Am. Chem. Soc.* **2017**, *139* (1), 47−50.

(14) Kim, D.; Resasco, J.; Yu, Y.; Asiri, A. M.; Yang, P. Synergistic Geometric and Electronic Effects for Electrochemical Reduction of Carbon Dioxide Using Gold-Copper Bimetallic Nanoparticles. *Nat. Commun.* **2014**, *5* (1), 4948.

(15) Zhou, Y.; Che, F.; Liu, M.; Zou, C.; Liang, Z.; De Luna, P.; Yuan, H.; Li, J.; Wang, Z.; Xie, H.; Li, H.; Chen, P.; Bladt, E.; Quintero-Bermudez, R.; Sham, T.-K.; Bals, S.; Hofkens, J.; Sinton, D.; Chen, G.; Sargent, E. H. Dopant-Induced Electron Localization Drives CO_2 Reduction to C_2 Hydrocarbons. *Nat. Chem.* **2018**, *10* (9), 974−980.

(16) Li, C. W.; Ciston, J.; Kanan, M. W. Electroreduction of Carbon Monoxide to Liquid Fuel on Oxide-Derived Nanocrystalline Copper. *Nature* **2014**, *508* (7497), 504−507.

(17) Xiao, H.; Goddard, W. A.; Cheng, T.; Liu, Y. Cu Metal Embedded in Oxidized Matrix Catalyst to Promote CO_2 Activation and CO Dimerization for Electrochemical Reduction of CO_2. *Proc. Natl. Acad. Sci. U. S. A.* **2017**, *114* (26), 6685−6688.

(18) Mariano, R. G.; McKelvey, K.; White, H. S.; Kanan, M. W. Selective Increase in CO_2 Electroreduction Activity at Grain-Boundary Surface Terminations. *Science* **2017**, *358* (6367), 1187−1192.

(19) Wang, Y.; Wang, Z.; Dinh, C.-T.; Li, J.; Ozden, A.; Golam Kibria, M.; Seifitokaldani, A.; Tan, C.-S.; Gabardo, C. M.; Luo, M.; Zhou, H.; Li, F.; Lum, Y.; McCallum, C.; Xu, Y.; Liu, M.; Proppe, A.; Johnston, A.; Todorovic, P.; Zhuang, T.-T.; Sinton, D.; Kelley, S. O.; Sargent, E. H. Catalyst Synthesis under CO_2 Electroreduction Favours Faceting and Promotes Renewable Fuels Electrosynthesis. *Nat. Catal.* **2020**, *3*, 98−106.

(20) Eddaoudi, M.; Kim, J.; Rosi, N.; Vodak, D.; Wachter, J.; O'Keeffe, M.; Yaghi, O. M. Systematic Design of Pore Size and Functionality in Isoreticular MOFs and Their Application in Methane Storage. *Science* **2002**, *295* (5554), 469−472.
(21) Jiang, J.; Furukawa, H.; Zhang, Y.-B.; Yaghi, O. M. High Methane Storage Working Capacity in Metal-Organic Frameworks with Acrylate Links. *J. Am. Chem. Soc.* **2016**, *138* (32), 10244−10251.
(22) Millward, A. R.; Yaghi, O. M. Metal-Organic Frameworks with Exceptionally High Capacity for Storage of Carbon Dioxide at Room Temperature. *J. Am. Chem. Soc.* **2005**, *127* (51), 17998−17999.
(23) Guntern, Y. T.; Pankhurst, J. R.; Vávra, J.; Mensi, M.; Mantella, V.; Schouwink, P.; Buonsanti, R. Nanocrystal/Metal-Organic Framework Hybrids as Electrocatalytic Platforms for CO_2 Conversion. *Angew. Chem., Int. Ed.* **2019**, *58* (36), 12632−12639.
(24) Diercks, C. S.; Liu, Y.; Cordova, K. E.; Yaghi, O. M. The Role of Reticular Chemistry in the Design of CO_2 Reduction Catalysts. *Nat. Mater.* **2018**, *17* (4), 301−307.
(25) Jiao, L.; Wang, Y.; Jiang, H.-L.; Xu, Q. Metal-Organic Frameworks as Platforms for Catalytic Applications. *Adv. Mater.* **2018**, *30* (37), 1703663.
(26) Nam, D.-H.; De Luna, P.; Rosas-Hernández, A.; Thevenon, A.; Li, F.; Agapie, T.; Peters, J. C.; Shekhah, O.; Eddaoudi, M.; Sargent, E. H. Molecular Enhancement of Heterogeneous CO_2 Reduction. *Nat. Mater.* **2020**, *19* (3), 266−276.
(27) Hou, S.-L.; Dong, J.; Zhao, B. Formation of C-X Bonds in CO_2 Chemical Fixation Catalyzed by Metal-Organic Frameworks. *Adv. Mater.* **2020**, *32* (3), 1806163.
(28) Albo, J.; Vallejo, D.; Beobide, G.; Castillo, O.; Castaño, P.; Irabien, A. Copper-Based Metal-Organic Porous Materials for CO_2 Electrocatalytic Reduction to Alcohols. *ChemSusChem* **2017**, *10* (6), 1100−1109.
(29) Albo, J.; Perfecto-Irigaray, M.; Beobide, G.; Irabien, A. Cu/Bi Metal-Organic Framework-Based Systems for an Enhanced Electrochemical Transformation of CO_2 to Alcohols. *J. CO_2 Util.* **2019**, *33*, 157−165.
(30) Kornienko, N.; Zhao, Y.; Kley, C. S.; Zhu, C.; Kim, D.; Lin, S.; Chang, C. J.; Yaghi, O. M.; Yang, P. Metal-Organic Frameworks for Electrocatalytic Reduction of Carbon Dioxide. *J. Am. Chem. Soc.* **2015**, *137* (44), 14129−14135.
(31) Nam, D.-H.; Bushuyev, O. S.; Li, J.; De Luna, P.; Seifitokaldani, A.; Dinh, C.-T.; Garcia de Arquer, F. P.; Wang, Y.; Liang, Z.; Proppe, A. H.; Tan, C. S.; Todorovic, P.; Shekhah, O.; Gabardo, C. M.; Jo, J. W.; Choi, J.; Choi, M.-J.; Baek, S.-W.; Kim, J.; Sinton, D.; Kelley, S. O.; Eddaoudi, M.; Sargent, E. H. Metal-Organic Frameworks Mediate Cu Coordination for Selective CO_2 Electroreduction. *J. Am. Chem. Soc.* **2018**, *140* (36), 11378−11386.
(32) Luan, Y.; Qi, Y.; Gao, H.; Andriamitantsoa, R. S.; Zheng, N.; Wang, G. A General Post-Synthetic Modification Approach of Amino-Tagged Metal-Organic Frameworks to Access Efficient Catalysts for the Knoevenagel Condensation Reaction. *J. Mater. Chem. A* **2015**, *3* (33), 17320−17331.
(33) Butova, V. V.; Budnyk, A. P.; Guda, A. A.; Lomachenko, K. A.; Bugaev, A. L.; Soldatov, A. V.; Chavan, S. M.; Øien-Ødegaard, S.; Olsbye, U.; Lillerud, K. P.; Atzori, C.; Bordiga, S.; Lamberti, C. Modulator Effect in UiO-66-NDC (1,4-Naphthalenedicarboxylic Acid) Synthesis and Comparison with UiO-67-NDC Isoreticular Metal-Organic Frameworks. *Cryst. Growth Des.* **2017**, *17* (10), 5422−5431.
(34) Xue, D.-X.; Belmabkhout, Y.; Shekhah, O.; Jiang, H.; Adil, K.; Cairns, A. J.; Eddaoudi, M. Tunable Rare Earth fcu-MOF Platform: Access to Adsorption Kinetics Driven Gas/Vapor Separations via Pore Size Contraction. *J. Am. Chem. Soc.* **2015**, *137* (15), 5034−5040.
(35) Cao, Y.; Zhao, Y.; Lv, Z.; Song, F.; Zhong, Q. Preparation and Enhanced CO_2 Adsorption Capacity of UiO-66/Graphene Oxide Composites. *J. Ind. Eng. Chem.* **2015**, *27*, 102−107.
(36) Hou, J.; Luan, Y.; Tang, J.; Wensley, A. M.; Yang, M.; Lu, Y. Synthesis of UiO-66-NH_2 Derived Heterogeneous Copper (II) Catalyst and Study of Its Application in the Selective Aerobic Oxidation of Alcohols. *J. Mol. Catal. A: Chem.* **2015**, *407*, 53−59.
(37) Tang, J.; Dong, W.; Wang, G.; Yao, Y.; Cai, L.; Liu, Y.; Zhao, X.; Xu, J.; Tan, L. Efficient Molybdenum(vi) Modified Zr-MOF Catalysts for Epoxidation of Olefins. *RSC Adv.* **2014**, *4* (81), 42977−42982.
(38) NIST. *NIST Chemistry WebBook, SRD 69*; NIST, 2018.
(39) Kuhl, K. P.; Hatsukade, T.; Cave, E. R.; Abram, D. N.; Kibsgaard, J.; Jaramillo, T. F. Electrocatalytic Conversion of Carbon Dioxide to Methane and Methanol on Transition Metal Surfaces. *J. Am. Chem. Soc.* **2014**, *136* (40), 14107−14113.
(40) Yang, Q.; Xu, Q.; Jiang, H.-L. Metal-Organic Frameworks Meet Metal Nanoparticles: Synergistic Effect for Enhanced Catalysis. *Chem. Soc. Rev.* **2017**, *46* (15), 4774−4808.
(41) Kung, C.-W.; Audu, C. O.; Peters, A. W.; Noh, H.; Farha, O. K.; Hupp, J. T. Copper Nanoparticles Installed in Metal-Organic Framework Thin Films Are Electrocatalytically Competent for CO_2 Reduction. *ACS Energy Lett.* **2017**, *2* (10), 2394−2401.
(42) Ghalei, B.; Wakimoto, K.; Wu, C. Y.; Isfahani, A. P.; Yamamoto, T.; Sakurai, K.; Higuchi, M.; Chang, B. K.; Kitagawa, S.; Sivaniah, E. Rational Tuning of Zirconium Metal-Organic Framework Membranes for Hydrogen Purification. *Angew. Chem., Int. Ed.* **2019**, *58* (52), 19034−19040.
(43) Popovych, N.; Kyriienko, P.; Soloviev, S.; Baran, R.; Millot, Y.; Dzwigaj, S. Identification of the Silver State in the Framework of Ag-Containing Zeolite by XRD, FTIR, Photoluminescence, ^{109}Ag NMR, EPR, DR UV-Vis, TEM and XPS Investigations. *Phys. Chem. Chem. Phys.* **2016**, *18* (42), 29458−29465.
(44) Schmitt, K. G.; Gewirth, A. A. In Situ Surface-Enhanced Raman Spectroscopy of the Electrochemical Reduction of Carbon Dioxide on Silver with 3,5-Diamino-1,2,4-Triazole. *J. Phys. Chem. C* **2014**, *118* (31), 17567−17576.
(45) Gao, J.; Zhang, H.; Guo, X.; Luo, J.; Zakeeruddin, S. M.; Ren, D.; Grätzel, M. Selective C-C Coupling in Carbon Dioxide Electroreduction via Efficient Spillover of Intermediates As Supported by Operando Raman Spectroscopy. *J. Am. Chem. Soc.* **2019**, *141* (47), 18704−18714.
(46) Duan, S.; Fang, P.-P.; Fan, F.-R.; Broadwell, I.; Yang, F.-Z.; Wu, D.-Y.; Ren, B.; Amatore, C.; Luo, Y.; Xu, X.; et al. A Density Functional Theory Approach to Mushroom-like Platinum Clusters on Palladium-Shell over Au Core Nanoparticles for High Electrocatalytic Activity. *Phys. Chem. Chem. Phys.* **2011**, *13* (12), 5441−5449.
(47) Gunathunge, C. M.; Ovalle, V. J.; Li, Y.; Janik, M. J.; Waegele, M. M. Existence of an Electrochemically Inert CO Population on Cu Electrodes in Alkaline PH. *ACS Catal.* **2018**, *8* (8), 7507−7516.
(48) Kas, R.; Kortlever, R.; Yılmaz, H.; Koper, M. T. M.; Mul, G. Manipulating the Hydrocarbon Selectivity of Copper Nanoparticles in CO_2 Electroreduction by Process Conditions. *ChemElectroChem* **2015**, *2*, 354.
(49) Liu, H.; Chu, J.; Yin, Z.; Cai, X.; Zhuang, L.; Deng, H. Covalent Organic Frameworks Linked by Amine Bonding for Concerted Electrochemical Reduction of CO_2. *Chem.* **2018**, *4* (7), 1696−1709.

https://dx.doi.org/10.1021/jacs.0c10774
J. Am. Chem. Soc. XXXX, XXX, XXX−XXX